Corrosion Science 189 (2021) 109589

Contents lists available at ScienceDirect

Corrosion Science

journal homepage: www.elsevier.com/locate/corsci

High temperature corrosion evaluation and lifetime prediction of porous Fe22Cr stainless steel in air in temperature range 700–900 °C

D. Koszelow [a,*], M. Makowska [b], F. Marone [b], J. Karczewski [c], P. Jasiński [a], S. Molin [a]

[a] Advanced Materials Centre, Faculty of Electronics, Telecommunications and Informatics, Gdańsk University of Technology, 80-233, Gdańsk, Poland
[b] Photon Science Division, Paul Scherrer Institut, Forschungsstrasse 111, 5232, Villigen, Switzerland
[c] Advanced Materials Centre, Faculty of Applied Physics and Mathematics, Gdańsk University of Technology, 80-233, Gdańsk, Poland

ARTICLE INFO

Keywords:
Stainless steel
High temperature corrosion
SEM
X-ray diffraction

ABSTRACT

This work describes a high temperature corrosion kinetics study of ~30 % porous Fe22Cr alloys. The surface area of the alloy (~0.02 $m^2\ g^{-1}$) has been determined by tomographic microscopy. The weight gain of the alloys was studied by isothermal thermogravimetry in the air for 100 h at 700–900 °C. Breakaway oxidation was observed after oxidation at 850 °C (~100 h) and 900 °C (~30 h). The lifetime prediction shows the investigated porous alloy can be used for >3000 h at temperatures <700 °C. At temperatures ≥700 °C, the lifetime of the porous alloy is limited by the available chromium reservoir.

1. Introduction

High temperature reactors and devices such as supercritical reactors, superheaters, turbines, and engines [1] rely on advanced alloys. For these applications, the most important properties of metallic alloys are their relatively low cost (in comparison to advanced ceramics), manufacturability, and the possibility to form complex shapes. In addition, high intrinsic electronic and heat conductivities can be beneficial for specific applications. For example, interconnects for high temperature (>600 °C) fuel cells require high electronic conductivity for efficient current collection and high heat conductivity to decrease thermal gradients. Ferritic stainless steels (FSSs), which are based on Fe and Cr, are the most common and cost-effective engineering alloys, being used in many room temperature and elevated temperature components (e.g. 430 alloy) [2]. For these reasons, the FSSs have been used as replacements for expensive and difficult to manufacture ceramic interconnects of the fuel cells [3–5]. To form a continuous chromia scale, the alloy should contain at least 10.5 wt.% Cr. Alloys with high chromium content (20−24 wt.%, e.g. Crofer 22 APU, Sanergy) have been designed to offer long term stable operation of the interconnects. Further increase of Cr content above ~26 wt.% is not beneficial, as it leads to a brittle sigma phase formation at high temperatures.

The drawback of using alloys at high temperatures in oxidising as well as in reducing (e.g. in H_2/H_2O) conditions is the unavoidable formation of metal oxide scales [6,7]. The most popular ferritic steels belong to the group of chromia formers, as they form chromium oxide (Cr_2O_3) on their surface [8]. The oxide has a protective function due to slow cation Cr^{3+} diffusion in the oxide, protecting the metallic core from rapid oxidation. Chromia has a satisfactory level of electrical conductivity (~1−10 mS cm^{-1} at 600−800 °C) [9] for applications requiring electrical current conduction, e.g. sensors, fuel cells, membranes. Silica or alumina forming ferritic alloys are typically less prone to high temperature oxidation, but they have negligible electronic conductivity, resulting in high electrical resistance of the oxide scale [10–13].

High temperature corrosion of alloys in the dense form has been studied for many decades and their properties are well described. More recently, porous metallic alloys became of greater interest as engineering materials for use at high temperatures. Due to open porosity, the porous alloys allow for gas transport, which is an important engineering feature. Porous ferritic stainless steels have been proposed as support structures for high temperature ceramic fuel cells [14–16] and gas separation membranes [17].

The porous structure of the alloy is characterized by a high surface area available for oxidation. The specific alloy powder particle size distribution determines the porosity and surface and thus it has a strong influence on the corrosion behavior of the porous components. The large area of the alloy available for oxidation, on which Cr_2O_3 will form, can cause relatively fast depletion of Cr from the bulk. Chromium depletion below a specific level will lead to breakaway oxidation. The threshold level of bulk Cr content for maintaining its protective action was

* Corresponding author.
E-mail address: damian.koszelow@pg.edu.pl (D. Koszelow).

https://doi.org/10.1016/j.corsci.2021.109589
Received 27 November 2020; Received in revised form 8 February 2021; Accepted 10 May 2021
Available online 27 May 2021

determined by Huczkowski et al. to be ~12 wt.% [18,19].

Several studies about the oxidation processes of the porous ferritic steels have been reported [20–26]. The existing studies point to relatively fast corrosion of porous alloys at high temperatures (≥800 °C), but the specific effects of the particle size, porosity, and surface area still remain open. The data is very limited in comparison to the number of studies of corrosion of the dense alloys.

The lifetime prediction for protective oxide scale forming alloys has also been already addressed by several authors with respect to different aspects. For example, Tucker et al. have discussed the lifetime as the time required to grow a ~3 μm thick oxide scale. Based on the reported corrosion values, the acceptable corrosion rates/temperatures have been mapped out [12]. Geometry-specific lifetime limitations for metallic alloys have been discussed by [18,27,28]. For example, Young et al. have devised a simple expression for lifetime prediction of austenitic (FCC) alloys [28]. Huczkowski et al. studied the effects of alloy sheet thickness on their lifetime [18].

This study describes the oxidation behavior of a sintered porous Fe22Cr alloy in the air at temperatures of 700 °C, 750 °C, 800 °C, 850 °C, and 900 °C. After the isothermal exposures, the sample microstructures were analyzed in detail. The results were used to propose a simple approach for the lifetime prediction of the porous alloy.

2. Experimental

The porous alloy substrates were obtained from the company: Höganäs AB (experimental product MW2, Höganäs, Sweden). Porous steel sheets were prepared by proprietary tape-casting of steel particle slurry, drying, debinding, and sintering. Before the corrosion exposures, an alloy sheet with dimensions of 100 × 100 × 0.4 mm^3 was cut into smaller pieces. For continuous thermogravimetric analysis, samples were cut into pieces with approximate dimensions of ~3 × 3 × 0.35 mm^3, where 3–4 pieces were placed simultaneously in the crucibles. For tomography, samples were cut into elongated samples with approximate dimensions of ~6 × 1 × 0.35 mm^3. Before further use, samples were cleaned in an ultrasonic bath of ethanol followed by acetone.

High-temperature corrosion exposures were performed using a Netzsch TG 209 F3 Tarsus thermobalance. Measurements were carried out in air with a flow rate of 50 mL min^{-1}. Used heating and cooling rates were 180 °C h^{-1}. An isothermal hold was maintained for 100 h at 700 °C, 750 °C, 800 °C, 850 °C and ~40 h at 900 °C (due to instabilities of the thermobalance for long measurements at high temperatures). Results were plotted as relative weight change, with respect to the weight of the samples before the oxidation. The typical initial weight of the samples was ~200 mg. The prediction of the alloy lifetime was based on the extrapolation of the weight gain data presented in the double logarithmic plot (which allowed fitting by linear regression). The confidence interval was determined by the prediction band method, assuming a 95 % confidence level.

Post-mortem characterizations were performed on samples prepared by ex-situ oxidation at conditions corresponding to isothermal exposures, i.e. the additional samples were oxidised continuously for 100 h at 700 °C, 750 °C, 800 °C, 850 °C, and 900 °C in parallel to thermogravimetric measurements. The characterization methods included scanning electron microscopy (SEM) evaluation using a Phenom XL (Thermo Fisher Scientific, Netherlands) instrument for observation of sample surfaces and polished cross-sections. A backscattered electron detector (BSE) was used for all SEM measurements. The qualitative elemental maps of the investigated samples were determined via energy-dispersive X-ray (EDX) spectroscopy using an integrated analyzer (Thermo Fisher Scientific, 25 mm^2 Silicon Drift Detector). Maps of Cr and Mn were made based on Cr K and Mn L lines. EDX "spot" analyses of the chemical composition, were performed by scanning a small area (maximum ~5 × 5 $μm^2$) to improve signal. The error bars of the EDX (in the case of chromium content data) were calculated as the standard deviation of the mean of 15 measurements carried out in different regions for each sample. Phase analysis was performed by X-ray diffractometry (XRD) using a Bruker D2 Phaser with an XE-T detector. XRD measurements were done using Cu anode (Kα =1.5405 Å), with 2Θ range 10 – 90° (step 0.02°, integration time 1 step s^{-1}). Cross-sections for SEM observations were prepared by embedding the samples in epoxy (EpoFix, Struers) and polishing them down to a 1 μm finish (Struers consumables).

X-ray tomographic microscopy characterization of samples was performed at TOMCAT beamline [29] of the the Swiss Light Source (SLS) at the Paul Scherrer Institute Villigen, Switzerland at the. Tomography scans of a reference (non-oxidised) sample and samples with different degrees of oxidation were performed using a parallel X-ray beam with energy of 40 keV. The detector setup consisted of a scintillator converting X-rays into visible light, an objective lens, and a sCMOS camera with settings providing a field of view (FOV) of about 0.8 mm x 0.8 mm with an image pixel size of 0.325 μm. 1001 projections over 180° were acquired with 1600 ms exposure time each, resulting in about 26 min scans.

The tomographic reconstruction pipeline [30] developed at the Tomcat group delivers full tomographic volumes immediately after data acquisition completion, which allows for prompt optimization of measurement and reconstruction algorithm parameters. The used reconstruction algorithm allows for partial phase retrieval according to the Paganin algorithm [31], which improves signal-to-noise and contrast-to-noise ratios. Reconstructed 3D volumes were analyzed using the commercial software Avizo 9.4 [32]. The information about sample porosity (open, closed, and total) and surface area was retrieved.

The porosity of porous alloys has also been determined experimentally by Archimedes principle (liquid displacement) and by image analysis. For image analysis, 20 pictures taken at a magnification of 2000x were analyzed using Phenom PoroMetricSoftware.

3. Results and discussion

3.1. Characterisation of the raw porous alloy

The surface morphology and cross-sectional microstructure of the "raw" sintered porous alloy are shown in Fig. 1A, B. The porous steel substrates used for the experiments were manufactured by Höganäs AB for potential application as support structures for high temperature fuel cells [33]. The main role of the relatively thick support is to provide mechanical strength for the much thinner (10−20x) ceramic layers and to enable good gas access to the electrodes. The presented porous metal sheet has a thickness of ~400 μm, similar to the ceramic/cermet supports used in traditional solid oxide cells [3]. The alloy particles used for the tape preparation were the -53 powder fraction (used sieve with 53 μm opening), resulting in particle sizes in the range of 10−50 μm. As seen in Fig. 1B, the particles are well connected and sintering necks between the particles are visible. The porosity of the metal sheet determined by the Archimedes method was ~30 % (±2 %), similar to the porosity of porous ceramic/cermet components used in fuel cells. Image analysis of the cross-section SEM image revealed a porosity of 31 % (±2%), which is in agreement with the Archimedes method.

The alloy is a ferritic (BCC crystallographic structure) stainless steel. As given by the alloy producer, the alloy contains ~22 wt.% of Cr, 0.23 wt.% Mn and 0.08 wt.% Si. Other elements include Ni, Cu, and Mo in amounts <0.03 wt.%. The chemical composition of the alloy, as given by the producer, is presented in Table 1. It is also confirmed by EDX analysis that shows ~21.3 wt.% Cr and 0.26 wt.% Mn plus iron as balance. At high temperatures, the metallic core is protected from heavy oxidation by a compact, slowly growing chromium oxide layer. High chromium content (~22.0 wt.%) should lead to an increased lifetime of the alloy due to an increased Cr reservoir available for the formation of the oxide scale. The addition of Mn can lead to the formation of the external Mn-Cr oxide spinel, which results in lower Cr evaporation [34,35]. Similar alloys, produced by Höganäs AB were used in other studies [24,25,33]. The alloy composition is quite similar to the state-of-the-art

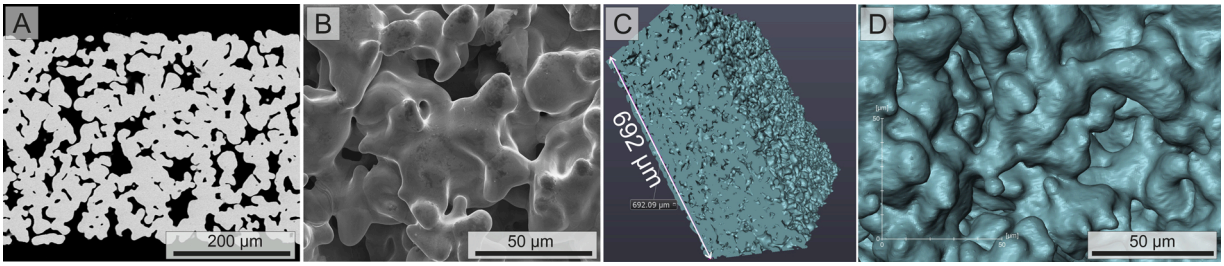

Fig. 1. SEM images of A) alloy cross section, B) surface and C, D) surface of the as-produced alloy generated from the tomographic reconstruction.

Table 1
Chemical composition of the alloy.

		Analyzed chemical composition, %										
Target composition	Fe	Cr	Ni	Mo	Mn	Cu	Si	Nb	C	O	N	S
Fe22Cr	Bal.	22.0	0.03	0.01	0.23	0.02	0.08	0.02	0.04	0.58	0.07	0.01

high temperature fuel cell alloys: Crofer 22 APU/H (VDM Metals, Germany) or Sanergy (Sandvik, Sweden).

To describe the complex microstructure of the non-oxidised porous alloys in more detail, tomographic microscopy was performed. The 3D microstructure of the alloy reconstructed from the series of projections is presented in Fig. 1C–D. Comparing Fig. 1B and D, the surface morphology obtained from tomography seems well reconstructed and is similar to that obtained via SEM. The porosity of the reference sample, obtained by the Avizo software is ~32.2 % and consists almost purely of open pores, which is in good agreement with the Archimedes-method and SEM measurements (~30 %). In the addition to porosity, the tomography allows for a calculation of the specific surface area, which is critical for the full assessment of corrosion properties at high temperatures. The specific surface area value obtained for the studied alloy was determined to be 0.022 $m^2\ g^{-1}$. The values can be compared with the available literature data. For example, Brandner has reported detailed processing of porous FeCr alloys in his PhD report [36]. He has obtained the surface area of ~0.02 $m^2\ g^{-1}$ for raw powders (gas atomized, SF 20−53_B2 – particle fraction 20−53 µm) used for sintering of porous alloys and a surface area of 0.007 $m^2\ g^{-1}$ for the ~18 % porous sintered product (sintering at 1250 °C for 3 h). Increasing the sintering temperature to 1350 °C led to a decrease of porosity to ~4 % and surface area to a level of ~0.001 $m^2\ g^{-1}$. In our work, the powders have been produced by a water atomization process (as evidenced by the irregular shape of the particles), which results in lower green density, thus higher resulting porosity and surface area after sintering. Stefan et al. have studied a porous FeCr alloy from the same producer, Höganäs AB. The authors analyzed the surface area by nitrogen absorption (BET) and reported a value of ~0.017 $m^2\ g^{-1}$, in line with our work [25]. Due to the relatively small amount of alloy availability, it was not possible to determine the BET area for our alloy. Rose et al. have also pointed out difficulties in determining the surface area of porous 430 alloys with the BET technique [37]. Due to the relatively low surface area of the porous alloys, the area determination is not simple due to the small amount of the adsorbed gas. In contrast to BET, tomography can be used on relatively small samples with good reproducibility, but its availability is much smaller and the data requires tedious post-processing.

In general, information about the specific surface area of the alloy is not easily obtainable. For comparison, a similar (chemical composition, thickness) dense alloy has a surface area of ~8 $cm^2\ g^{-1}$, a factor of ~28x smaller. This shows a striking difference in the surface area available for oxide formation on porous alloys.

3.2. Corrosion exposures of porous alloys

The as-produced alloys were subjected to isothermal oxidation exposures in the air at temperatures of 700 °C, 750 °C, 800 °C, 850 °C, and 900 °C. Weight gain measurement results are shown in Fig. 2. The weight gain is shown as a relative weight gain (with respect to the initial sample weight) as well as is recalculated for the surface area, using the specific surface value determined by tomography. As the determination of the specific surface area (SSA) of porous alloys is troublesome, many research works only report the relative weight gain (% change). This data is, however, only relevant to the specific microstructure and a comparison between different publications, working with different materials is not possible quantitatively. Only a few works report surface specific weight gain data for porous alloys, which also makes it possible to compare the obtained oxidation kinetics data with the data available from oxidation of dense alloys.

The results presented in Fig. 2 show that the exposure temperature has a strong effect on the oxidation kinetics. Oxidation at 900 °C progresses very fast. After only ~25 h the slope of the weight gain curve changed (Fig. 2A), the oxidation process accelerated, whereby suggesting that a breakaway oxidation process started. Sample oxidised ex-situ at 900 °C for 100 h showed a weight gain of ~43 %, which corresponds to oxidation of all Fe and Cr. For the oxidation at 850 °C, the weight gain is initially following a parabolic-type (weight gain ~ square root of time) curve, which after ~40 h seems to become linear. The weight gain curves obtained at 800 °C, 750 °C and 700 °C seem to follow the parabolic rate law. The weight gain at 700 °C after 100 h of oxidation is the only $1/10^{th}$ of the weight gain obtained at 800 °C.

In order to determine the oxidation mechanism in more detail, Fig. 2B shows a double logarithmic plot (log-log plot) of the weight gain as a function of time. For the diffusion limited corrosion kinetics, the slope of the log-log plot should be 0.5. The rate determining factor, in this case, is typically outward cation diffusion. Our data shows good agreement throughout the measured time range. For all temperatures, the slopes are similar, confirming that the parabolic rate law ($\left(\frac{\Delta m}{A}\right)^2 = k_p * t$, where A is surface of the sample, Δm is a change of sample`s mass, k_p is the parabolic rate constant and t is a time of oxidation) can be used for the description of corrosion kinetics.

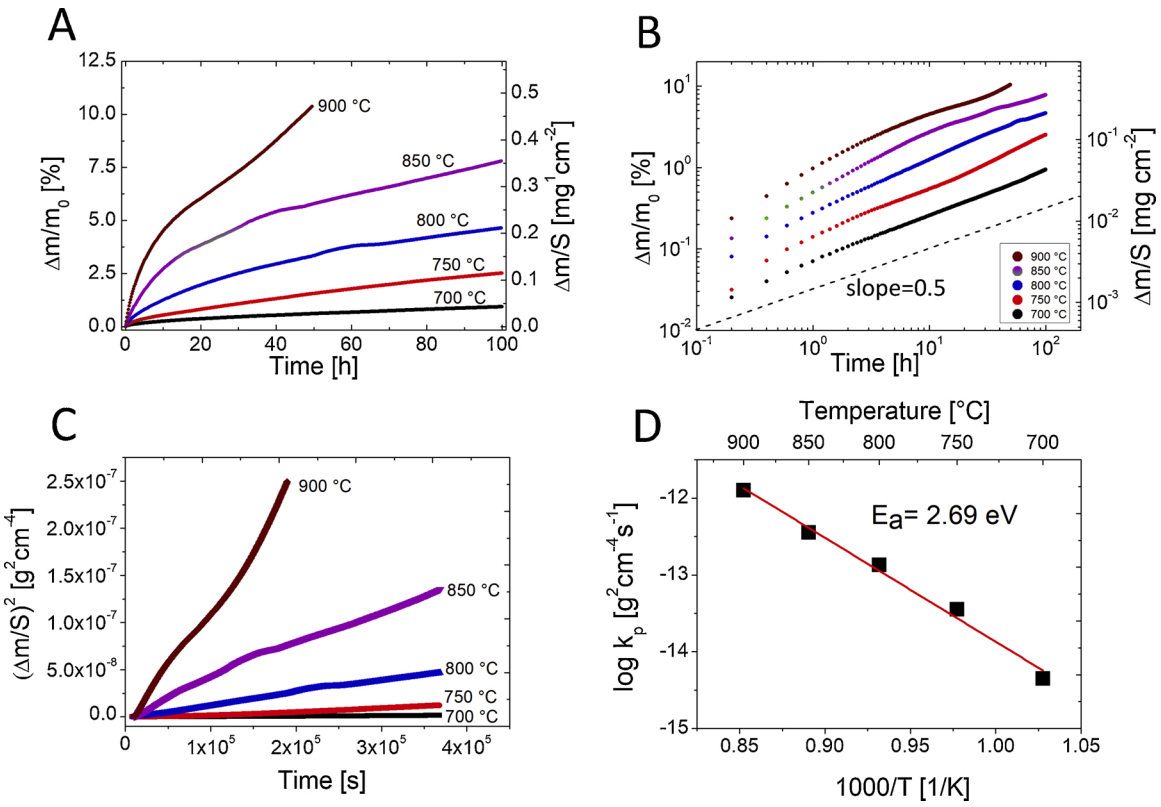

Fig. 2. Weight gain data presented as A) linear weight change, B) log-log plot, C) square weight change with respect to the initial surface area and D) Arrhenius plot.

Table 2
Corrosion parameters after oxidation at different temperatures.

Temperature	Weight gain @ 100 h		Corrosion rate – k_p	$k_{p\ temp}$ / $k_{p\ 700\ °C}$	Activation energy
°C	%	mg cm^{-2}	g^2 cm^{-4} s^{-1}		eV
900 (40 h)	10.4	0.50	1.3×10^{-12}	289	
850	7.80	0.37	3.7×10^{-13}	82	
800	4.65	0.22	1.3×10^{-13}	28	2.69
750	2.52	0.11	3.6×10^{-14}	8	
700	0.94	0.04	4.5×10^{-15}	1	

Based on the assumption of the parabolic rate law, Fig. 2C shows parabolic weight gain plots (per surface area) for the alloys. The calculated corrosion rates (k_p values - slopes of the curves) are presented in Table 2. For comparison, for the FeCr porous alloy studied by Stefan et al., the k_p values of 8×10^{-15} g^2 cm^{-4} s^{-1} at 700 °C and 1×10^{-12} g^2 cm^{-4} s^{-1} at 800 °C were obtained [25]. The values are typical, as reported for chromia forming ferritic stainless steels [2]. The obtained values can be compared with a porous Al-forming alloy. In the case of FeCrAlY porous alloy (with comparable particle size) studied by Glasscock et al., the corrosion rate obtained at 850 °C was ~4×10^{-16} g^2 cm^{-4} s^{-1}. The corrosion rate of the Al-former is thus ~3 orders of magnitude lower than for the Cr-former. Unfortunately, the former cannot be used in applications where electronic conduction of the support is required. In other applications, like in oxygen transport membranes (OTM), alumina forming alloys have a clear advantage. For comparison with the results reported for dense alloys, Gavrilov et al. determined the parabolic rate constant for the Crofer 22 APU to be 5.6×10^{-14} g^2 cm^{-4} s^{-1} after 100 h oxidation at 800 °C [38]. Skilbred et al. calculated this parameter for Sandvik Sanergy HT at 800 °C as 5.4×10^{-14} g^2 cm^{-4} s^{-1} [39]. For Crofer 22 H alloy, the values are 4.5×10^{-16}, 1.1×10^{-14} and 3.3×10^{-13} g^2 cm^{-4} s^{-1} for 650, 750 and 850 °C, respectively [40].

Overall the weight gain and corrosion kinetics k_p values obtained for the porous alloys in our work are in good agreement with the available corrosion data for chromia forming alloys. Due to minor compositional differences (e.g. Cr content, reactive elements, etc.), some variation of k_p values between different alloys is possible [41].

The calculated corrosion rate values were used to determine the activation energy of the oxidation process. The plot of k_p vs the inverse of the temperature is presented in Fig. 2D. The points follow a line with the activation energy of ~2.7 eV. As cited by Palcut et al., the activation energy of Cr diffusion in Cr_2O_3 is ~2.9 eV (280 kJ mol^{-1}) [42], therefore the obtained value corresponds well with the assumed Cr diffusion oxidation rate limitation.

For dense alloys, Palcut et al. has obtained an activation energy of ~2.5 eV for Crofer 22 APU alloy [43], and for a similar Sanergy alloy, Skilbred et al. calculated an activation energy of 2.82 eV [39]. In general, the obtained value corresponds well with the expected one.

3.3. *Post-mortem analysis of porous alloys*

SEM images of the surfaces of the alloys oxidised for 100 h at 700 °C, 750 °C, 800 °C, 850 °C, and 900 °C are presented in Fig. 3A–I.

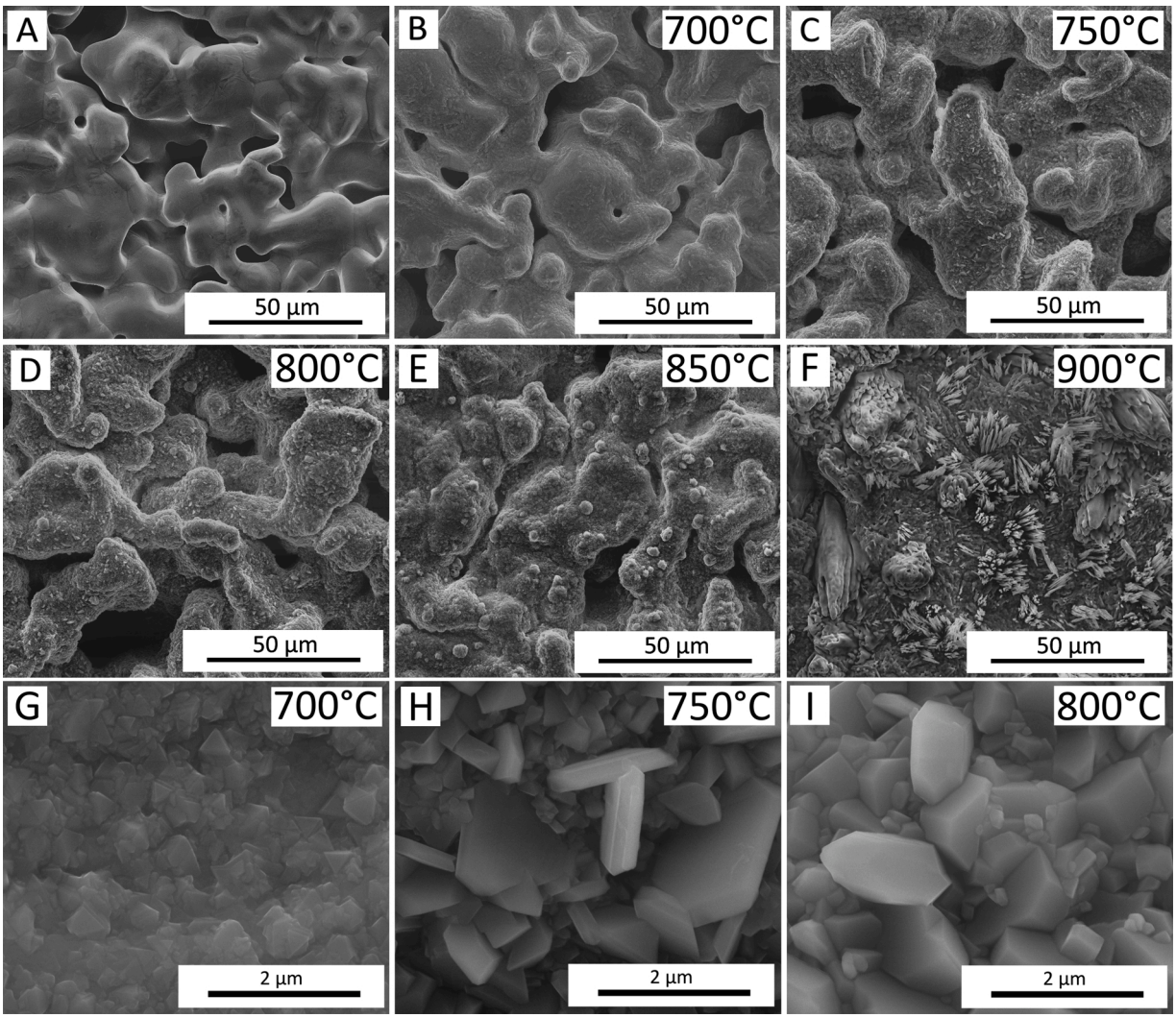

Fig. 3. SEM surface of samples A) non-oxidised; oxidised for 100 h at B, G) 700 °C, C, H) 750 °C, D, I) 800 °C, E) 850 °C and F) 900 °C.

The surface of the alloy oxidised at 700 °C shows, at low magnification, only slight changes in comparison to the not-oxidised alloy. The higher magnification shown in Fig. 3G reveals the formation of small (<1 µm), densely packed crystallites on the surface. The alloys oxidised at 750 °C and 800 °C show a clear change of the surface, which becomes rougher, but still, no large changes of the alloy microstructure are observed, i.e. pores are clearly visible. Higher magnification images (Fig. 3H and I) show the growth of larger crystallites. Especially at 750 °C, the platelet

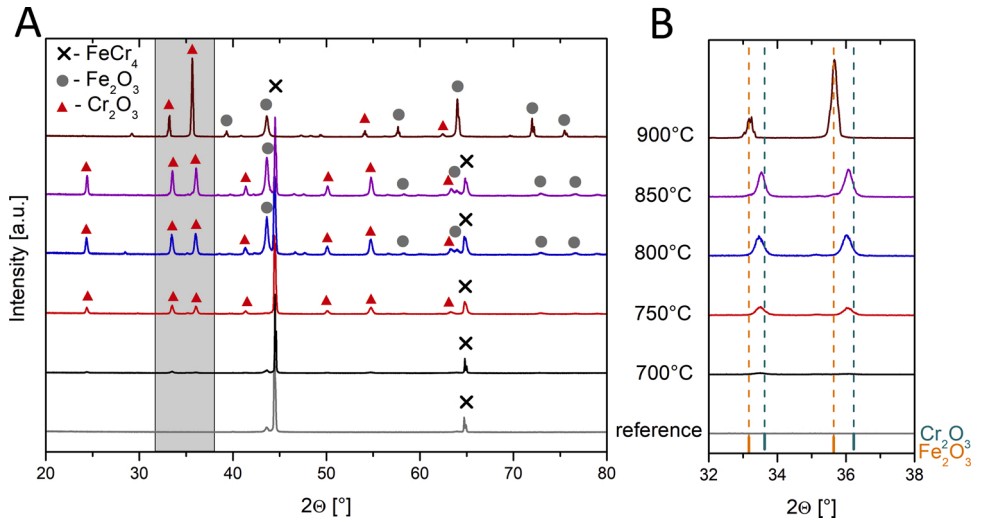

Fig. 4. XRD patterns of the reference and oxidised alloys: A) full range scan 20-80°, B) magnification of the 32-38° range.

shape of the larger crystals growing from a layer of smaller crystals is visible. At 800 °C, the crystallites grow further. Severe microstructure change occurred for the alloy oxidised at 850 °C and 900 °C. High temperature leads to a porosity decrease. In the case of the alloy oxidised at 900 °C, a dense surface is visible. The alloy was completely oxidised, with no features of the initial porous alloy remaining.

The oxidation temperature thus has an effect not only on the amount of the oxide (as determined by the weight gain) but also on the crystallite's morphology. Oxide scales with different crystallite sizes can have an effect on cation diffusion since the relative amount of grains and grain boundaries will be altered.

Surface morphological studies were followed by phase analysis using XRD. The measured diffraction patterns, for samples oxidised at 700 °C, 750 °C, 800 °C, 850 °C, and 900 °C for 100 h are presented in Fig. 4A–B. A reference pattern of the non-oxidised steel has also been included (CrFe4, ICDD PDF number 65-4664).

The alloy oxidised at 700 °C for 100 h shows only a minor peak at the position of the main peak of the Cr_2O_3 phase (ICDD PDF number 38-1479), visible in Fig. 4B. For the alloy oxidised at 750 °C for 100 h, new phases clearly formed, however the main alloy peak at ~45° is the most intense.

The oxide peaks can be matched well to the Cr_2O_3 and possibly to Fe_2O_3 (ICDD PDF number 33-664) phases, which have similar structures and diffractograms. Peaks are shifted, most likely due to iron doping of the oxide phase or due to experimental conditions (sample displacement). For the samples oxidised at 800 °C (and higher) shifting of the peaks towards the Fe_2O_3 reference, the position could be observed. The sample oxidised at 900 °C shows only peaks from the oxide phase, whereby the metallic substrate is not detectable anymore.

The enlargement of the main oxide peak area, presented in Fig. 4B, shows good agreement of the oxide position with the Fe_2O_3 peaks for the sample oxidised at 900 °C. For the other temperatures, there seems to be a mixed $(Fe,Cr)_2O_3$ oxide.

Due to the small Mn content in the alloy (~0.2 wt.%), possibly also Mn,Cr spinel could form, but its presence was not detected in this study.

SEM images of cross-sections of samples oxidised at 700 °C, 750 °C, and 800 °C are presented in Fig. 5A–F. The low-magnification images (Fig. 5A, B, C) show a lack of changes in the overall microstructure. The

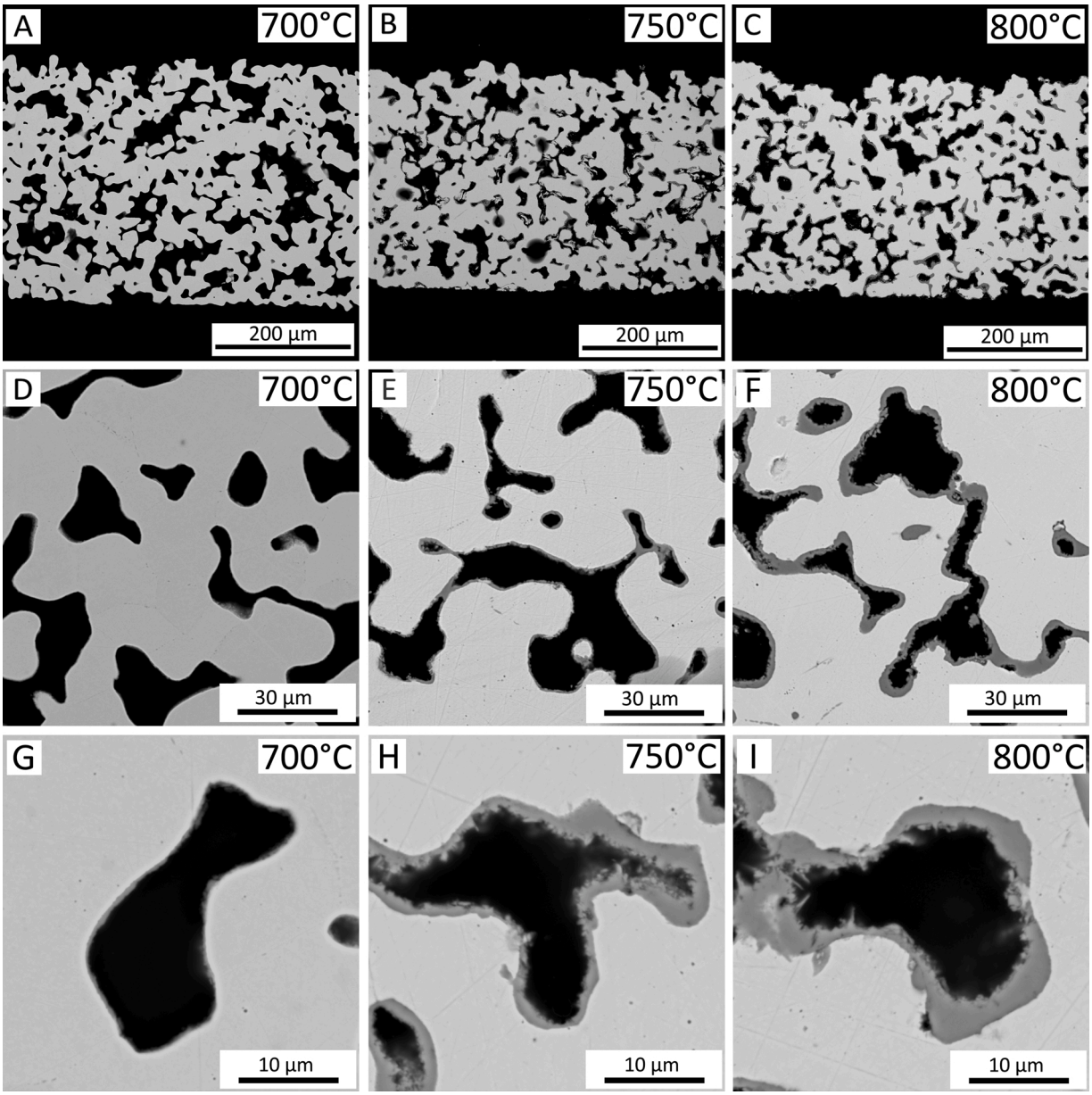

Fig. 5. SEM cross-section images of the alloy oxidised for 100 h at A,D,G) 700 °C, B,E,H) 750 °C, C,F,I) 800 °C.

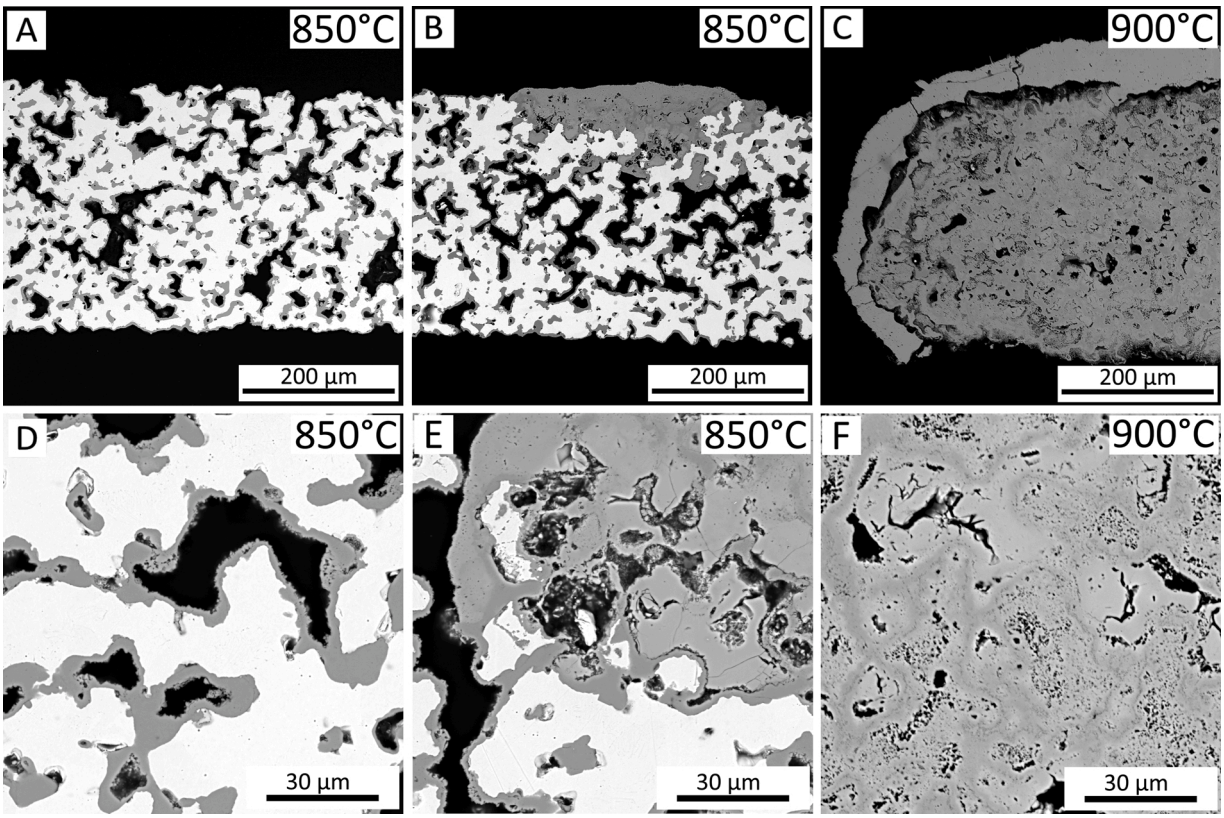

Fig. 6. SEM cross-section images of the alloy oxidised for 100 h at A, D) 850 °C in place without breakaway corrosion, B, E) 850 °C for 100 h in a place with breakaway corrosion and C, F) 900 °C for 100 h.

sample oxidised at 700 °C for 100 h, with the relative weight gain of ~1% (~0.05 mg cm^{-2}), shows no visible change in comparison to the not-aged sample (Fig. 1). Even at higher magnification (Fig. 5D and G), the formation of the oxide scale is hardly visible. For a sample oxidised at 750 °C, with a weight gain of ~2.5 % (~0.11 mg cm^{-2}), the thin layer of oxide is noticeable at lower magnifications (Fig. 5B and E). At higher magnification (Fig. 5H), a small amount oxide is clearly visible, but it does not block the pores. The sample oxidised at 800 °C, with a weight gain of ~5% (~0.21 mg cm^{-2}), when observed at the lowest magnification (Fig. 5C) shows hardly visible oxide that formed within the pores, whereas when observed at higher magnifications (Fig. 5F and I), the oxide becomes easily visible on the surface of grains. A continuous oxide layer covers uniformly the whole surface, with a thickness of 2–3 µm. The pores decrease in size due to oxide scale growth filling the available space.

The cross-section images of samples oxidised at 850 °C and 900 °C for 100 h are presented in Fig. 6A–F. Most of the sample oxidised at 850 °C (Fig. 6A), characterised by a ~7.5 % weight gain (~0.35 mg cm^{-2}), did not show signs of breakaway oxidation. Excessive oxidation could be obtained, however, in at least one place along the studied cross-section (Fig. 6B). As seen in the higher magnification image (Fig. 6D), the oxidation at 850 °C leads to formation of the clearly visible oxide scale. The oxide fills the pores to a measurable extent and starts filling the small pores (necks) between the grains. The oxide scale covers the surface well, no scale detachment, delamination or cracking is visible. The breakaway spot is formed near the surface/edge of the sample. The heavily oxidised region extends ~200 µm in width and penetrates up to ~100 µm in depth. The rapid oxidation of Fe can explain the observed linear weight gain curve (Fig. 2A), but due to the relatively small extent (very limited number of spots) of the breakaway corrosion, it did not dominate the overall weight gain trend.

The sample that was exposed to 900 °C for 100 h, with a weight gain of ~43 % (~2 mg cm^{-2}), shows only the oxide phase, no metallic particles could be found in SEM images. The sample shows a relatively dense microstructure, with a very dense shell around the sample core.

To determine the chemical composition of the oxide scale and the breakaway region, the EDX analysis was performed for the cross-section of the sample oxidised at 850 °C for 100 h. Two regions were analyzed: one where no breakaway oxidation was found (Fig. 7A) and a second one, with a visible breakaway corrosion spot (Fig. 7B).

The oxide scale is composed of Cr and O, which supplemented by the XRD results suggest formation of a pure Cr_2O_3 scale. Due to the presence of a minor amount of Mn in the alloy (~0.2 wt.%), the potential formation of an $(Mn,Cr)_3O_4$ spinel could be expected. However, even though a thorough analysis was performed, it did not show the formation of the spinel phase. As seen in Fig. 7A, the Mn signal (qualitative) is mostly concentrated inside the grains, so this seems to be an artefact coming from EDX fitting. Additional higher magnification analyses (not shown here) did not reveal any signs of Mn-rich oxide on top of chromia. The amount of Mn in the studied alloy is lower than in Crofer 22 APU (Mn ~0.4 wt.%) which might be crucial in forming a continuous spinel scale.

The breakaway spot, presented in Fig. 7B, shows high iron, chromium, and oxygen content (Table 3). Region 1, representing the alloy composition after oxidation, shows a Cr content of ~10 at.% with the remaining Fe. The alloy core has been thus heavily depleted from the

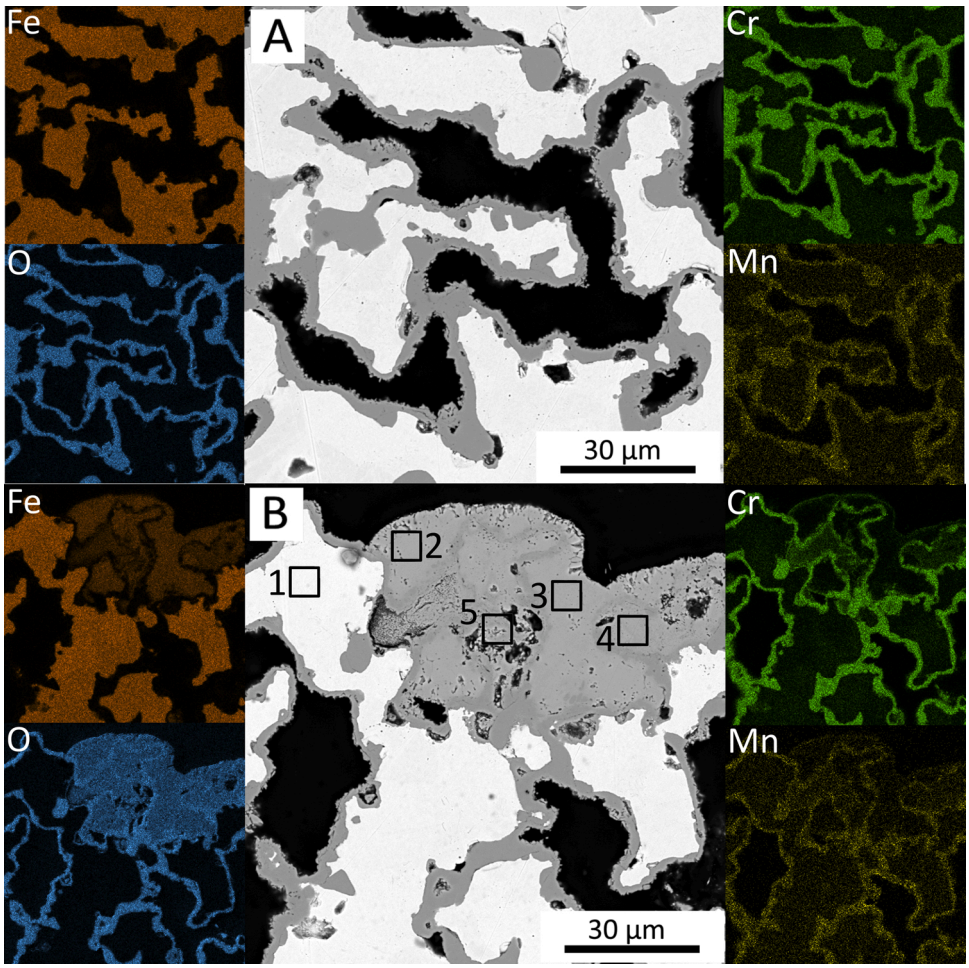

Fig. 7. EDX analysis(qualitative maps) of sample oxidised at 850 °C for 100 h. A) place without breakaway corrosion, B) place with breakaway corrosion.

Table 3
Chemical composition of regions marked in Fig. 7 B(obtained from EDX measurements).

Region	Fe at. %	Cr at. %	Mn at. %	O at. %
1	90.3	9.7	<0.1	–
2	34.5	1.7	<0.1	63.8
3	33.5	2.5	<0.1	63.9
4	28.0	7.1	–	64.9
5	20.7	13.9	0.2	65.2

initial ~21 wt.% of Cr content. Region 2, inside the breakaway zone, is mainly composed of iron (~34 at.%) with low Cr content (< 2at.%) with oxygen as balance. A similar composition is obtained for regions 3 and 4. Region 5 shows both high concentrations of iron, chromium, and oxygen. Analysing the breakaway region of the elemental map presented in Fig. 7B, it seems that Cr is mainly contained in a layer, that initially covered the steel grains. At some point, the Cr depleted grains started to oxidise, forming iron rich oxides. The chromia layer remained relatively stable and thus its structure is retained within the formed oxide.

The breakaway corrosion originated near to the external surface of the porous alloy and only in a few spots. For the particles near the external surface of the alloy, the incoming flux of the Cr will be limited spatially, so the formation of breakaway corrosion closer to the surface than to the middle can be rationalised. Another considered possibility is Cr evaporation from the external surface, whereas in the internal surfaces the atmosphere would get saturated faster. Similarly, the differences in water and oxygen availability for places near the surface of the alloy might also affect breakaway corrosion appearance in these regions.

In addition to SEM microscopy, tomographic studies of selected samples (not-oxidised, oxidised at 800 °C for 100 h and 900 °C for 30 h) were performed. Fig. 8 presents results of material segmentation of the reconstructed volumes showing the distribution of different phases. For the oxidised samples, it was possible to distinguish between the metallic core, the oxide, and the porosity phases. To the best of our knowledge, it is the first time such observations were made. Obtaining high contrast between the materials considered in this paper and high spatial resolution using X-rays with energy sufficient for penetration of this type of samples (about 1 mm steel) remains a challenge. The thin oxide layer can be resolved using synchrotron radiation, thanks to its high brilliance and partial coherence. Therefore, it was possible to obtain sufficient contrast between the oxide layer and the metallic phase as well as submicron spatial resolution. The differentiation of the phases can be used to quantitatively measure the extent of corrosion based on 3D microstructure, enhancing the information obtained by SEM.

For the sample oxidised at 800 °C for 100 h (weight gain of ~4.65 %), the oxide is observed uniformly covering the steel particles, no breakaway corrosion was found within the investigated volume, in-line with SEM observations. For the sample oxidised at 900 °C for 30 h (weight gain of ~7%), the oxide forms several breakaway spots. Based on the images, the volume of the three phases can be calculated. The data is presented in Table 4. Based on the results, it is visible that upon the oxidation, the metallic phase transforms into the oxide phase at the expense of porosity. For the sample oxidised at 800 °C for 100 h, the steel volume decreased from the initial ~68 % to 63 %, the open porosity decreased from the initial ~32 % to ~21 % and the oxide phase

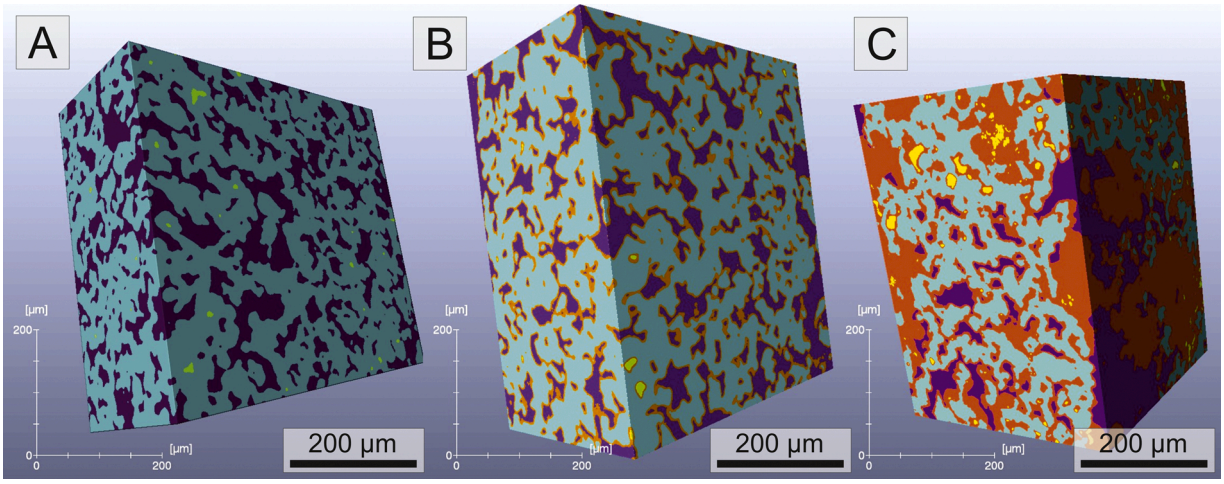

Fig. 8. Phase segmentation based on synchrotron tomography of samples: A) before oxidation, B) oxidised for 100 h at 800 °C and C) oxidised for 30 h at 900 °C (turquoise – steel, orange-oxide, purple – open pores, green- closed pores).

Table 4
Summary of the phase composition of selected samples evaluated based on tomography data.

Temperature	Time	Figure	Steel vol%	Oxide vol%	Open porosity vol%	Closed porosity vol%
–	–	Fig. 8 A	67.7	–	32.2	0.1
800 °C	100 h	Fig. 8 B	62.8	16.6	20.5	0.1
900 °C	30 h	Fig. 8 C	46.3	41.0	11.3	1.4

contributes with ~17 % of the total volume. Based on the densities of the steel (7.7 g cm^{-3}) and the oxide (chromia density of 5.22 g cm^{-3}), the measured decrease of the steel phase corresponds theoretically to ~16 % oxide volume, which agrees well with the value determined by the tomography.

For the sample oxidised at 900 °C for 30 h, the oxide phase constitutes 41 % of the total volume, with the remaining low porosity of ~11 %.

As seen in Figs. 7B and 8 C, the breakaway corrosion of porous alloys leads to large microstructural changes of the alloys and is limiting their applications. For the specific alloy used in this study, it occurs within times as short as ~100 h at 850 °C and even shorter at higher temperatures. It would be beneficial to develop models, predicting the lifetime of porous alloys so that their use within the safe limits would be possible.

3.4. Lifetime prediction of porous alloys

Based on the obtained oxidation kinetics results, a rough lifetime prediction can be made. The prediction is relevant to the specific alloy (in terms of its microstructure and chemical composition), but the methodology can be used for other alloys as well. The advantage of the method is its relative simplicity, but on the other hand, it requires assuming some critical weight gain limit, at which the start of breakaway corrosion is supposed to.

The method presented here is only an approximation of complex oxidation phenomena and should be treated as a simplified methodology only. The prediction is based on the extrapolation of the weight gain data, presented in Fig. 2B. Based on the weight gain curves and microscopic/tomographic observations, it can be assumed that the breakaway oxidation starts at a weight gain of ~6 %. For the alloy oxidised at 800 °C the weight gain reached ~5 % after 100 h and no breakaway oxidation was found in the SEM post-mortem analyses. For the sample oxidised at 850 °C, the weight gain after 100 h reached 7.5 % and the breakaway corrosion already started. For the oxidation at 900 °C, a change of weight gain slope can be observed at ~6 %. Therefore this weight gain value has been selected as a potential start of the breakaway corrosion.

The log-log weight gain plot can be used to extrapolate the linear curves to reach the weight gain limit of ~6 %, which would be the lifetime limit – time before the breakaway oxidation can be expected (Fig. 9A). The data for 900 °C and 850 °C seems to fit within the proposed model. For the lower temperatures, the predicted lifetimes are 136 ± 20 h for 800 °C, 395 ± 50 h for 750 °C and 2916 ± 170 h for 700

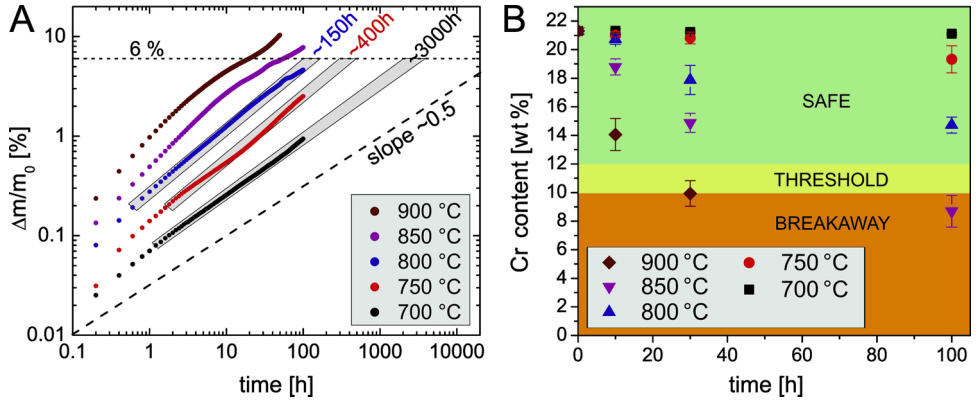

Fig. 9. A) Log-log extrapolation of weight gain and B) chromium content in the alloy determined by EDX.

°C. The predicted lifetimes seem quite low. For high temperature fuel cells, the desired lifetimes of the stacks are within the 10000−40000 hours range (for mobile and stationary systems, respectively). Therefore it seems that the porous alloys with the presented chemical composition and microstructure should be operated at temperatures lower than 700 °C. Alternatively, specially tailored protective coatings could be developed.

The measured weight gain is due to oxygen pick up, which can be calculated into Cr consumption. A rough estimation yields a value of ~13 wt.% Cr consumed (corresponding to 9 wt.% Cr remaining in the bulk). This estimation is in good agreement with the EDX analysis of the oxidised alloy, which was 9.7 % (region 1 in Fig. 7B). The Cr content in the alloys after different stages of oxidation was analysed by EDX and the results are plotted in Fig. 9B. The figure has been color-coded into three regions – based on the obtained results the operation of the porous alloy is safe (green area) down to ~12 wt.% Cr content below which some smaller particles can be oxidised heavily. For a Cr content <10 wt. %, most of the alloy will be heavily oxidised (orange area).

The obtained lifetime predictions are roughly in-line with some of the literature reports. The discussion of the applicability of the proposed lifetime prediction based on the available literature data is hard due to differences in porous metal morphology and compositions. Moreover, there is yet not much data about oxidation of porous alloys.

Huczkowski et al. have studied the oxidation of flat Crofer 22 APU alloys with different thicknesses [18]. Based on the measured corrosion rates, the lifetime of Crofer 22 APU at 800 °C was ~8000 h for 100 μm sample thickness. Extrapolated to a thickness of 50 μm, the lifetime would be only ~3000 h. The planar, 2D geometry makes a large difference from the spherical grain geometry. Chyrkin et al. have studied the oxidation and lifetime of Inconel 625 (austenitic alloy) foams with different particle sizes. For the foams made with small particles (~10 μm), oxidation lifetimes as low as ~100 h at 900 °C were obtained experimentally and used to validate the model. By increasing the particle size to ~30 μm, the lifetime could be increased to 400−500 h. The model predicts that a temperature decrease to 700 °C can lead to a lifetime above 10000 h.

Shen et al. have performed long term durability tests of metal-supported solid oxide electrolysis cells. In their design, the cell has porous metal sheets on both sides (hydrogen/steam and air/oxygen). The employed steel is based on a 434 composition, which has 16−18 wt. % Cr. The authors performed ~1000 h long aging test. The authors did not observe breakaway oxidation within the studied period. The oxide scale thickness has been determined to be ~2 μm for the air side and ~1 μm for the hydrogen side. Brandner has reported in his PhD thesis, oxidation results of ~18 % porous Crofer 22 APU sheets [36]. The experiments were carried out in air at 800 °C. The surface specific weight gain after 1000 h was ~0.5 mg cm^{-2}. Based on his observations, the lifetime of such alloy has been predicted to be between 200−500 h -relatively short for possible practical application. Schiller et al. have presented a ~2400 h long test for a porous metal-supported electrolysis cell carried out at 800 °C [44]. The porous metal substrate was based on Plansee ITM alloy (Fe based, ~26 wt.% Cr, with the addition of ~1 wt.% Y_2O_3). The porous metal support did not undergo breakaway oxidation within the test time, which seems to survive much longer than our simple prediction. Though the microstructure and composition of the alloy were quite similar to that studied here, the support was exposed to a reducing atmosphere (hydrogen/steam). Exposures in reducing atmospheres result in lower corrosion rates than in air, which seems especially visible in the case of porous alloys [25,45]. Also, the addition of even a small amount of Y_2O_3 might play a major role in extending the alloy lifetime in harsh conditions [46].

Due to the complex geometry of the porous alloys and foams, their oxidation limited lifetime is much shorter than for dense alloys. To fully develop a reliable lifetime model for porous alloys, more long-term, controlled condition exposure studies are needed, also including samples with different microstructures.

Lifetime prediction is a complex problem, depending heavily on the potential failure mode, alloy composition, and microstructure. In the present work, results indicate that the lifetime was limited by Cr depletion. Failure due to oxide detachment due to reaching a critical oxide thickness and stress level cannot be excluded.

4. Conclusions

This work has evaluated short term (~100 h) high temperature corrosion properties of a ~30 % porous Fe22Cr alloy in the temperature range 700 °C – 900 °C. To determine the specific surface area, synchrotron tomographic microscopy was applied. This technique allowed obtaining the surface value (~0.022 m^2 g^{-1}) from a relatively small sample. The corrosion results demonstrate that the corrosion rate of porous alloys is similar to corrosion rates of dense alloys, i.e. the complex shape has no visible effect on the underlying corrosion phenomena. The corrosion kinetics is acceptable at 700 °C, whereas at higher temperatures the alloy microstructure changes considerably even after only 100 h of exposure. Oxidation of samples at 850 °C and 900 °C leads to breakaway corrosion and the alloy becomes fully oxidised after 100 h at 900 °C. The tomographic analysis was also performed on oxidised alloys and it allowed for a determination of the relative content of the steel/oxide/pore phases. Using tomography, it is possible to analyse 3D microstructures of the alloys quantitatively, which strongly supplements the weight gain and microscopic analyses. 3D visualization achieved from tomographic microscopy gives also a better insight into the amount distribution of breakaway spots as compared with 2D imaging.

Based on the obtained experimental results, a methodology for lifetime prediction has been proposed. Based on the experimentally derived critical oxidation level (weight gain of ~6%), a double logarithmic plot was used to extrapolate the data from lower temperatures. The predicted lifetime at 700 °C is ~3000 h, which is relatively short. The results show that there is a need for longer term studies, which will be the focus of our future work.

CRediT authorship contribution statement

D. Koszelow: Investigation, Methodology, Data curation, Visualization, Writing - original draft. **M. Makowska:** Writing - review & editing, Formal analysis, Validation. **F. Marone:** Writing - review & editing, Software, Validation. **J. Karczewski:** Validation, Data curation. **P. Jasiński:** Methodology, Resources, Supervision. **S. Molin:** Conceptualization, Methodology, Writing - original draft, Supervision, Funding acquisition.

Declaration of Competing Interest

The authors report no declarations of interest.

Acknowledgments

This project was supported by National Science Centre Poland (NCN) Sonata Bis 8 project number 2018/30/E/ST8/00821 “High-temperature corrosion studies and development of oxidation lifetime model of alloy powders and sintered porous alloys: effects of composition and microstructure”.

The authors would like to acknowledge Höganäs AB, Sweden for porous steel samples production and the Paul Scherrer Institut, Villigen, Switzerland for granting beamtime (proposal 20181598) at the TOMCAT beamline of the Swiss Light Source.

References

[1] D.J. Young, High Temperature Oxidation and Corrosion of Metals, Elsevier, 2008.
[2] M.C. Tucker, Progress in metal-supported solid oxide fuel cells: a review, J. Power Sources 195 (2010) 4570–4582, https://doi.org/10.1016/j.jpowsour.2010.02.035.
[3] S. Linderoth, Solid oxide cell R&D at Risø National Laboratory—and its transfer to technology, J. Electroceram. 22 (2009) 61–66, https://doi.org/10.1007/s10832-008-9458-6.
[4] M.C. Tucker, G.Y. Lau, C.P. Jacobson, L.C. DeJonghe, S.J. Visco, Stability and robustness of metal-supported SOFCs, J. Power Sources 175 (2008) 447–451, https://doi.org/10.1016/j.jpowsour.2007.09.032.
[5] M.C. Tucker, Durability of symmetric-structured metal-supported solid oxide fuel cells, J. Power Sources 369 (2017) 6–12, https://doi.org/10.1016/j.jpowsour.2017.09.075.
[6] L. Niewolak, D.J. Young, H. Hattendorf, L. Singheiser, W.J. Quadakkers, Mechanisms of oxide scale formation on ferritic interconnect steel in simulated low and high pO2 service environments of solid oxide fuel cells, Oxid. Met. 82 (2014) 123–143, https://doi.org/10.1007/s11085-014-9481-8.
[7] T. Thublaor, S. Chandra-ambhorn, High temperature oxidation and chromium volatilisation of AISI 430 stainless steel coated by Mn-Co and Mn-Co-Cu oxides for SOFC interconnect application, Corros. Sci. 174 (2020), 108802, https://doi.org/10.1016/j.corsci.2020.108802.
[8] L.-P. Wang, W. Yang, Z.-B. Ma, J.-H. Zhu, Y.-T. Li, First-principles study of chromium diffusion in the ferritic Fe-Cr alloy, Comput. Mater. Sci. 181 (2020), 109733, https://doi.org/10.1016/j.commatsci.2020.109733.
[9] A. Holt, P. Kofstad, Electrical conductivity and defect structure of Cr2O3. II. Reduced temperatures (<~1000°C), Solid State Ion. 69 (1994) 137–143, https://doi.org/10.1016/0167-2738(94)90402-2.
[10] R. Wang, Z. Sun, J.-P. Choi, S.N. Basu, J.W. Stevenson, M.C. Tucker, Ferritic stainless steel interconnects for protonic ceramic electrochemical cell stacks: oxidation behavior and protective coatings, Int. J. Hydrogen Energy 44 (2019) 25297–25309, https://doi.org/10.1016/j.ijhydene.2019.08.041.
[11] M.A. Hassan, O. Bin Mamat, M. Mehdi, Review: Influence of alloy addition and spinel coatings on Cr-based metallic interconnects of solid oxide fuel cells, Int. J. Hydrogen Energy 45 (2020) 25191–25209, https://doi.org/10.1016/j.ijhydene.2020.06.234.
[12] M.C. Tucker, Progress in metal-supported solid oxide electrolysis cells: a review, Int. J. Hydrogen Energy 45 (2020) 24203–24218, https://doi.org/10.1016/j.ijhydene.2020.06.300.
[13] A. Persdotter, J. Eklund, J. Liske, T. Jonsson, Beyond breakaway corrosion – influence of chromium, nickel and aluminum on corrosion of iron-based alloys at 600 °C, Corros. Sci. 177 (2020), 108961, https://doi.org/10.1016/j.corsci.2020.108961.
[14] B. Timurkutluk, S. Toros, S. Onbilgin, H.G. Korkmaz, Determination of formability characteristics of Crofer 22 APU sheets as interconnector for solid oxide fuel cells, Int. J. Hydrogen Energy 43 (2018) 14638–14647, https://doi.org/10.1016/j.ijhydene.2018.04.243.
[15] N.J. Magdefrau, L. Chen, E.Y. Sun, M. Aindow, Effects of alloy heat treatment on oxidation kinetics and scale morphology for Crofer 22 APU, J. Power Sources 241 (2013) 756–767, https://doi.org/10.1016/j.jpowsour.2013.03.181.
[16] P. Alnegren, M. Sattari, J. Froitzheim, J.E. Svensson, Degradation of ferritic stainless steels under conditions used for solid oxide fuel cells and electrolyzers at varying oxygen pressures, Corros. Sci. 110 (2016) 200–212, https://doi.org/10.1016/j.corsci.2016.04.030.
[17] J.A. Glasscock, L. Mikkelsen, Å.H. Persson, G. Pećanac, J. Malzbender, P. Blennow, F. Bozza, P.V. Hendriksen, Porous Fe21Cr7Al1Mo0.5Y metal supports for oxygen transport membranes: thermo-mechanical properties, sintering and corrosion behaviour, Solid State Ion. 242 (2013) 33–44, https://doi.org/10.1016/j.ssi.2013.04.006.
[18] P. Huczkowski, V. Shemet, J. Piron-Abellan, L. Singheiser, W.J. Quadakkers, N. Christiansen, Oxidation limited life times of chromia forming ferritic steels, Mater. Corros. 55 (2004) 825–830, https://doi.org/10.1002/maco.200303798.
[19] P. Huczkowski, N. Christiansen, V. Shemet, J. Piron-Abellan, L. Singheiser, W. J. Quadakkers, Oxidation induced lifetime limits of chromia forming ferritic interconnector steels, J. Fuel Cell Sci. Technol. 1 (2004) 30, https://doi.org/10.1115/1.1782925.
[20] J.A. Glasscock, V. Esposito, S.P.V. Foghmoes, T. Stegk, D. Matuschek, M.W.H. Ley, S. Ramousse, The effect of forming stresses on the sintering of ultra-fine Ce0.9Gd0.1O2−δ powders, J. Eur. Ceram. Soc. 33 (2013) 1289–1296, https://doi.org/10.1016/j.jeurceramsoc.2012.12.015.
[21] Y. Matus, L. Dejonghe, C. Jacobson, S. Visco, Metal-supported solid oxide fuel cell membranes for rapid thermal cycling, Solid State Ion. 176 (2005) 443–449, https://doi.org/10.1016/j.ssi.2004.09.056.
[22] D.N. Boccaccini, H.L. Frandsen, B.R. Sudireddy, P. Blennow, Å.H. Persson, K. Kwok, P. Vang Hendriksen, Creep behaviour of porous metal supports for solid oxide fuel cells, Int. J. Hydrogen Energy 39 (2014) 21569–21580, https://doi.org/10.1016/j.ijhydene.2014.07.138.
[23] G. Reiss, H.L. Frandsen, W. Brandstätter, A. Weber, Numerical evaluation of microstructural parameters of porous supports in metal-supported solid oxide fuel cells, J. Power Sources 273 (2015) 1006–1015, https://doi.org/10.1016/j.jpowsour.2014.09.185.
[24] M. Stange, C. Denonville, Y. Larring, A. Brevet, A. Montani, Improvement of corrosion properties of porous alloy supports for solid oxide fuel cells, Int. J. Hydrogen Energy 42 (2017) 12485–12495, https://doi.org/10.1016/j.ijhydene.2017.03.170.
[25] E. Stefan, C. Denonville, Y. Larring, M. Stange, R. Haugsrud, Oxidation study of porous metal substrates for metal supported proton ceramic electrolyzer cells, Corros. Sci. 164 (2020), 108335, https://doi.org/10.1016/j.corsci.2019.108335.
[26] M. Mokhtari, T. Wada, C. Le Bourlot, J. Duchet-Rumeau, H. Kato, E. Maire, N. Mary, Corrosion resistance of porous ferritic stainless steel produced by liquid metal dealloying of Incoloy 800, Corros. Sci. 166 (2020), 108468, https://doi.org/10.1016/j.corsci.2020.108468.
[27] C. Asensio-Jimenez, L. Niewolak, H. Hattendorf, B. Kuhn, P. Huczkowski, L. Singheiser, W.J. Quadakkers, Effect of Specimen Thickness on the Oxidation Rate of High Chromium Ferritic Steels: The Significance of Intrinsic Alloy Creep Strength, Oxid. Met. (n.d.) 1–14. https://doi.org/10.1007/s11085-012-9323-5.
[28] D.J. Young, A. Chyrkin, W.J. Quadakkers, A simple expression for predicting the oxidation limited life of thin components manufactured from FCC high temperature alloys, Oxid. Met. 77 (2012) 253–264, https://doi.org/10.1007/s11085-012-9283-9.
[29] G. Lovric, R. Mokso, C.M. Schlepütz, M. Stampanoni, A multi-purpose imaging endstation for high-resolution micrometer-scaled sub-second tomography, Phys. Med. 32 (2016) 1771–1778, https://doi.org/10.1016/j.ejmp.2016.08.012.
[30] F. Marone, A. Studer, H. Billich, L. Sala, M. Stampanoni, Towards on-the-fly data post-processing for real-time tomographic imaging at TOMCAT, Adv. Struct. Chem. Imaging 3 (2017) 1–11, https://doi.org/10.1186/s40679-016-0035-9.
[31] D. Paganin, S.C. Mayo, T.E. Gureyev, P.R. Miller, S.W. Wilkins, Simultaneous phase and amplitude extraction from a single defocused image of a homogeneous object, J. Microsc. 206 (2002) 33–40, https://doi.org/10.1046/j.1365-2818.2002.01010.x.
[32] D Visualization & Analysis Software, (n.d.).
[33] H. Gschiel, C. Gierl-Mayer, H. Danninger, P.-O. Larsson, H. Vidarsson, Manufacturing and microstructure of porous metal supports for a solid oxide fuel cell, Powder Metall. 58 (2015) 178–181, https://doi.org/10.1179/0032589915Z.000000000237.
[34] R. Sachitanand, M. Sattari, J.E. Svensson, J. Froitzheim, Evaluation of the oxidation and Cr evaporation properties of selected FeCr alloys used as SOFC interconnects, Int. J. Hydrogen Energy 38 (2013) 15328–15334, https://doi.org/10.1016/j.ijhydene.2013.09.044.
[35] M. Park, J.-S. Shin, S. Lee, H.-J. Kim, H. An, H. Ji, H. Kim, J.-W. Son, J.-H. Lee, B.-K. Kim, H.-W. Lee, K.J. Yoon, Thermal degradation mechanism of ferritic alloy (Crofer 22 APU), Corros. Sci. 134 (2018) 17–22, https://doi.org/10.1016/j.corsci.2018.01.022.
[36] M. Brandner, Verbundstruktur für Hochtemperatur- brennstoffzellen in mobilen Anwendungen, 2006.
[37] L. Rose, O. Kesler, C. Decès-Petit, T. Troczynski, R. Maric, Characterization of porous stainless steel 430 for low- and intermediate-temperature solid oxide fuel cell (SOFC) substrates, Int. J. Green Energy 6 (2009) 638–645, https://doi.org/10.1080/15435070903372510.
[38] N.V. Gavrilov, V.V. Ivanov, A.S. Kamenetskikh, A.V. Nikonov, Investigations of Mn-Co-O and Mn-Co-Y-O coatings deposited by the magnetron sputtering on ferritic stainless steels, Surf. Coat. Technol. 206 (2011) 1252–1258, https://doi.org/10.1016/j.surfcoat.2011.08.036.
[39] A.W.B. Skilbred, R. Haugsrud, Sandvik Sanergy HT - A potential interconnect material for LaNbO 4-based proton ceramic fuel cells, J. Power Sources 206 (2012) 70–76, https://doi.org/10.1016/j.jpowsour.2012.01.101.
[40] H. Falk-Windisch, J.E. Svensson, J. Froitzheim, The effect of temperature on chromium vaporization and oxide scale growth on interconnect steels for Solid Oxide Fuel Cells, J. Power Sources 287 (2015) 25–35, https://doi.org/10.1016/j.jpowsour.2015.04.040.
[41] J.W. Fergus, Metallic interconnects for solid oxide fuel cells, Mater. Sci. Eng. A 397 (2005) 271–283, https://doi.org/10.1016/j.msea.2005.02.047.
[42] M. Palcut, L. Mikkelsen, K. Neufeld, M. Chen, R. Knibbe, P.V. Hendriksen, Corrosion stability of ferritic stainless steels for solid oxide electrolyser cell interconnects, Corros. Sci. 52 (2010) 3309–3320, https://doi.org/10.1016/j.corsci.2010.06.006.
[43] M. Palcut, L. Mikkelsen, K. Neufeld, M. Chen, R. Knibbe, P.V. Hendriksen, Corrosion stability of ferritic stainless steels for solid oxide electrolyser cell interconnects, Corros. Sci. 52 (2010) 3309–3320.
[44] G. Schiller, A. Ansar, M. Lang, O. Patz, High temperature water electrolysis using metal supported solid oxide electrolyser cells (SOEC), J. Appl. Electrochem. 39 (2009) 293–301, https://doi.org/10.1007/s10800-008-9672-6.
[45] S. Molin, B. Kusz, M. Gazda, P. Jasinski, Evaluation of porous 430L stainless steel for SOFC operation at intermediate temperatures, J. Power Sources 181 (2008) 31–37, https://doi.org/10.1016/j.jpowsour.2007.10.009.
[46] S. Molin, M. Gazda, P. Jasinski, Coatings for improvement of high temperature corrosion resistance of porous alloys, J. Eur. Ceram. Soc. 31 (2011) 2707–2710, https://doi.org/10.1016/j.jeurceramsoc.2011.02.007.